Non-PCR Ultrasensitive Detection of Viral RNA by a Nanoprobe-Coupling Strategy: SARS-CoV-2 as an Example

Zhiguo Yu, Wenming Fang, Yannan Yang, Heliang Yao, Ping Hu,* and Jianlin Shi*

Developing efficient and highly sensitive diagnostic techniques for early detections of pathogenic viruses such as Severe Acute Respiratory Syndrome Coronavirus 2 (SARS-CoV-2) is vitally important for preventing its widespread. However, the conventional polymerase chain reaction (PCR)-based detection features high complexity, excessive time-consumption, and labor-intensiveness, while viral protein-based detections suffer from moderate sensitivity and specificity. Here, a non-PCR but ultrasensitive viral RNA detection strategy is reported based on a facile nanoprobe-coupling strategy without enzymatic amplification, wherein PCR-induced bias and other shortcomings are successfully circumvented. This approach endows the viral RNA detection with ultra-low background to maximum signal ratio in the linear signal amplification by using Au nanoparticles as reporters. The present strategy exhibits 100% specificity toward SARS-CoV-2 N gene, and ultrasensitive detection of as low as 52 cp mL^{-1} of SARS-CoV-2 N gene without pre-PCR amplification. This approach presents a novel ultrasensitive tool for viral RNA detections for fighting against COVID-19 and other types of pathogenic virus-caused diseases.

1. Introduction

Coronavirus disease 2019 (COVID-19) caused by the novel coronavirus SARS-CoV-2, has spread widely around the world, leading to a global pandemic.[1] Wide-scale screening and isolation of infected patients are the most effective way to control the ongoing SARS-CoV-2 pandemic. Thus, efforts to develop efficient and sensitive diagnosis techniques for the early detection of SARS-CoV-2 in asymptomatic stage with no obvious symptoms are highly significant for transmission prevention. Since the COVID-19 outbreak, several biosensing systems for SARS-CoV-2 detection have been developed, including the protein-based detection[2] and nucleic acid-based detection.[3] Viral protein-based technologies, including the enzyme-linked immunosorbent assay (ELISA), the lateral flow assays, and gold immunochromatography assay[4] features the direct identification of specific protein on the surface of the virus without multiple steps of RNA extraction and enzymatic amplification, but suffers from moderate sensitivity and specificity.[5]

As a gold standard for the diagnosis of SARS-CoV-2 infection, the quantitative real time polymerase chain reaction (qRT-PCR)[3b] is widely used in clinical detection of viral nucleic acid.[6] Despite marked progresses in the virus nucleic acid detection technology,[2a,3a,7] PCR-based detection assays are still criticized for their complexity, long time-consumption, high cost, and labor-intensiveness, which makes the operators at the high risk of infection.[8] Normally, molecular diagnosis using clinical qRT-PCR detection takes at least 4 h, including a series of complicated steps such as RNA concentration determination, RNA reverse transcription (convert RNA to cDNA), cDNA dilution, PCR amplification system configuration, and cycle amplification reaction.[9] Moreover, the relatively low efficiency of viral RNA preparation leads to much reduced sensitivity of detection due to the inevitable RNA degradation by nuclease.[10] Of note, an increasing number of false negativity reports[11] of qRT-PCR has been observed in the SARS-CoV-2 diagnoses for asymptomatically infected and convalescent patients most recently.[12] No doubt, a remarkably faster and more sensitive methodology than the existing PCR-like signal amplification without the major drawbacks of PCR will contribute greatly to the pandemic prevention and eventual elimination.

Herein, we report a non-PCR but efficient and ultrasensitive approach to detect SARS-CoV-2 RNA with the aid of specific

Z. Yu, W. Fang, H. Yao, P. Hu, J. Shi
State Key Laboratory of High Performance Ceramics and Superfine Microstructure
Shanghai Institute of Ceramics Chinese Academy of Sciences; Research Unit of Nanocatalytic Medicine in Specific Therapy for Serious Disease
Chinese Academy of Medical Sciences (2021RU012)
Shanghai 200050, P. R. China
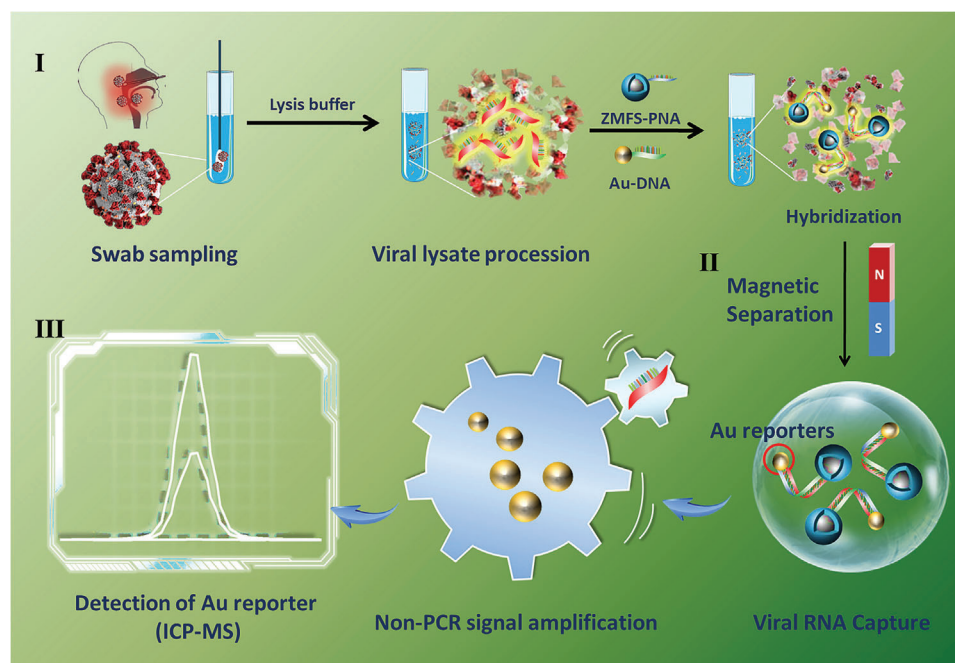E-mail: huping@mail.sic.ac.cn; jlshi@mail.sic.ac.cn

Z. Yu, W. Fang
Center of Materials Science and Optoelectronics Engineering
University of Chinese Academy of Sciences
Beijing 100049, P. R. China

P. Hu, J. Shi
Shanghai Tenth People's Hospital
Shanghai Frontiers Science Center of Nanocatalytic Medicine
School of Medicine
Tongji University
Shanghai 200331, P. R. China

Y. Yang
Australian Institute for Bioengineering and Nanotechnology
The University of Queensland
St Lucia, Brisbane, Queensland 4072, Australia

**ADVANCED
SCIENCE NEWS**

www.advancedsciencenews.com

**ADVANCED
HEALTHCARE
MATERIALS**

www.advhealthmat.de

Figure 1. Schematic diagram of nanoprobe-coupling strategy (NCS) for SARS-CoV-2 detection. I) Samples are collected with a swab, then vortexed and split to prepare lysis solutions; II) ZnMnFe$_2$O$_4$@SiO$_2$-PNA (ZMFS-PNA) and Au-DNA hybridize with SARS-CoV-2 N gene resulting in nanoprobe coupling, and the coupled nanoprobes are collected by magnetic separation; III) NCS signal output amplified by using Au nanoparticles as reporters via ICP-MS.

hybridization reactions between two captures DNA/PNA strands respectively grafted on magnetic iron oxide and gold nanoprobes, and the target RNA strand (**Figure 1**). This strategy starts with the pretreatment of samples, followed by the capture of target RNA, and finally converts the RNA detection into highly efficient Au quantification of extremely low detection limit, by which the target SARS-CoV-2 N gene can be ultrasensitively detected and quantified in a linear relation with the measured amount of Au nanoparticles (Au NPs). With the efficient magnetic separation and enrichment of target RNA and the ultra-low theoretical detection limit (30 cp mL^{-1}) of Au ions by inductively coupled plasma mass spectrometer (ICP-MS),[13] this nanoparticle-coupling assay features linear signal outputs from low background to maximum amplified one by using Au NPs as reporters.[14] This strategy features greatly enhanced sensitivity and specificity for the viral RNA detection, by which extremely low concentrations of 52 cp mL^{-1} of SARS-CoV-2 N gene have been quantified, in comparison with the common detection limits of ≈500 cp mL^{-1} of popular clinical qRT-PCR test.[15] This novel methodology is herein named as nanoprobe-coupling strategy (NCS).
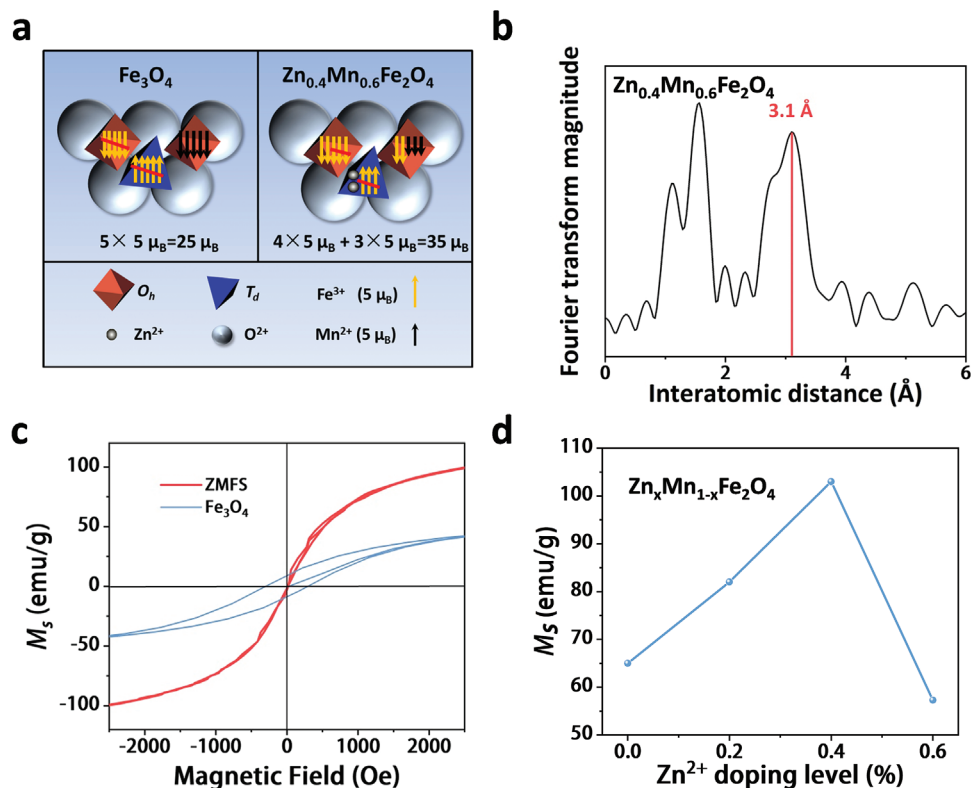
2. Results and Discussion

The design protocol of the NCS for the separation and quantitative detection of SARS-CoV-2 RNA is shown in Figure 1, which consists of two kinds of nanoprobes ZnMnFe$_2$O$_4$@SiO$_2$-PNA (ZMFS-PNA) and Au-DNA. As an initial demonstration of the NCS assay, we first focus on the detection of the fragments, the most specific sequence of the SARS-CoV-2 N gene.[7a] The complementary strands to the target N gene strand were divided into two half sequences, named as capture DNA and PNA, which

were then modified on the surfaces of magnetic nanoparticles and gold nanoparticles respectively. Sequences used in this work were indicated in Table S1, Supporting Information. In the target N gene-containing solution, both types of nanoparticle probes can specifically hybridize with the target N gene strand by these two capture sequences. In this way, two nanoprobes (ZMFS-PNA and Au-DNA) would be coupled together by such classic DNA hybridization reactions.[16]

The SARS-CoV-2 N gene bridged ZMFS-PNA and Au-DNA nanoprobe-coupling system was then magnetically separated and then re-dispersed in solution, and finally measured the Au concentration by ICP-MS, which was then used to determine the N gene level by pre-establishing a linear correlation between the target N gene and Au concentration as the standard calibration curve. In this NCS assay, magnetic nanoparticles were used to rapidly separate and enrich the target N gene-positive RNA, whlie Au nanoprobe was to transfer, amplify and output the detection signal.

The magnetic nanoprobes in this assay with excellent biocompatibility and magnetic separation/enrichment performances are crucial to the detection results. Traditional Fe$_3$O$_4$ nanoparticles have been developed for decades,[17] but the less sufficient nanomagnetism and poor dispersion can hardly satisfy the rapid and accurate detections of extremely trace biomarkers. In this regard, a metal substitution strategy for Fe$_3$O$_4$ (metal ferrite) nanoparticles has been considered to obtain largely strengthened nanomagnetism. Of note, Mn^{2+} has a larger average magnetic moment than Fe^{2+} in Fe$_3$O$_4$, and Zn^{2+} doping further elevates the saturation magnetization of the nanoparticles.[18]

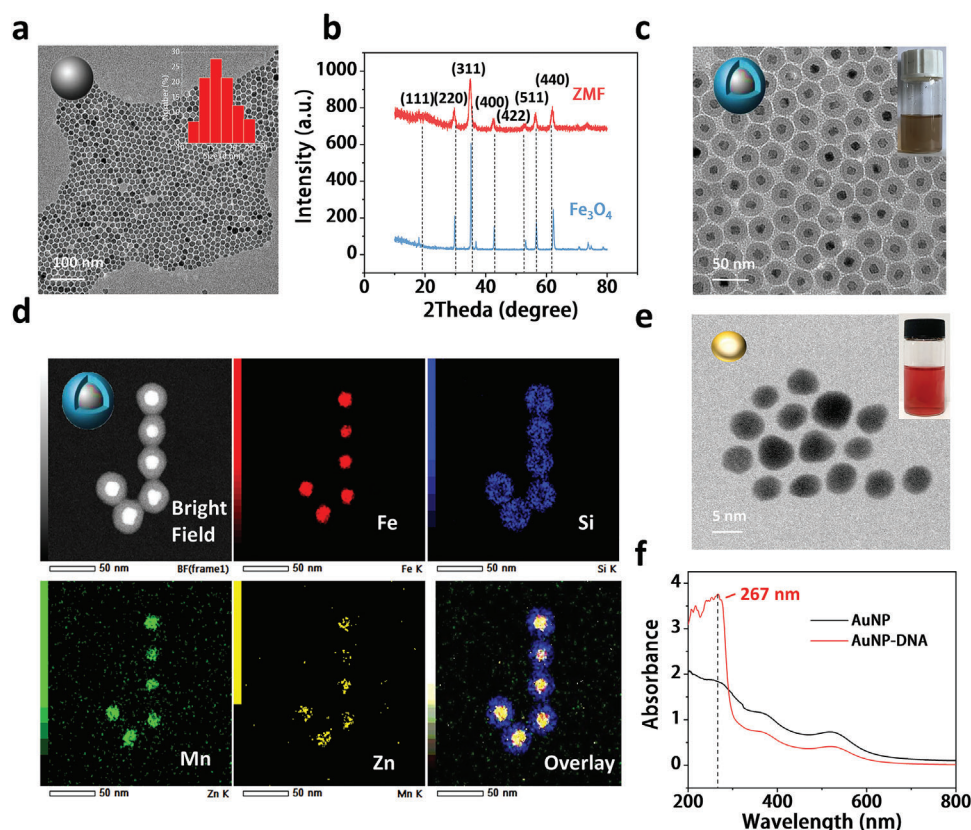Herein, we synthesized Zn^{2+}/Mn^{2+} doped metal ferrite ZMF NPs and explored the mechanism of magnetic property

ADVANCED
SCIENCE NEWS
www.advancedsciencenews.com

ADVANCED
HEALTHCARE
MATERIALS
www.advhealthmat.de

Figure 2. a) Undoped and Zn^{2+} doped ($x = 0.4$) magnetic spin alignment diagrams of $Zn_xMn_{1−x}Fe_2O_4$. b) Zn K-edge EXAFS spectra of $Zn_{0.4}Mn_{0.6}Fe_2O_4$ nanoparticles. c) Hysteresis curves of $Zn_{0.4}Mn_{0.6}Fe_2O_4$ and Fe_3O_4 nanoparticles. d) Plot of M_s versus Zn^{2+} doping level of $Zn_xMn_{1−x}Fe_2O_4$ nanoparticles.

enhancement by doping zinc atoms. The Zn^{2+} doping levels were tuned by varying the molecule ratio of the metal acetyl acetone precursor to iron species. As illustrated in the crystalline structure of ZMF (Figure S1, Supporting Information), the doped Zn^{2+} ions mostly occupy the T_d sites of the spinel structure. By this doping, the change of antiferromagnetic coupling interactions resulted in the enhancement of the nanoparticle's magnetism. The occupancy of Zn^{2+} ions at the T_d sites induced the partial removal of antiferromagnetic coupling interactions between Fe^{3+} ions in O_h and T_d sites (**Figure 2**a). The local atomic environment and charge state of the doped Zn ions in ZMF NPs were further confirmed by extended X-ray absorption fine structure (EXAFS) analyses. As shown in Figure 2b, the Fourier-transformed peak at 3.1 Å in the Zn K-edge EXAFS spectra originates from the central Zn^{2+} ions at T_d sites. The magnetism of ZMF magnetic nanoparticles was measured using a physical property measurement system (PPMS) at 300 K. The saturation magnetizations of Fe_3O_4 NPs (18 nm) have been determined to be around 50 emu $g^{−1}$. In contrast, that of ZMF NPs (18 nm) reaches over 100 emu $g^{−1}$ (Figure 2c), indicating the substantial magnetization enhancement by Mn^{2+} and Zn^{2+} co-doping. Additionally, the saturation magnetization of ZMF increases with the increase of Zn^{2+} doping level. At the Zn^{2+} doping amounts of $x = 0$, 0.2, and 0.4, the corresponding saturation magnetization intensities of $Zn_xMn_{1−x}Fe_2O_4$ are 65, 82, 102 emu $g^{−1}$, respectively (Figure 2d). However, the saturation magnetization intensity of $Zn_xMn_{1−x}Fe_2O_4$ decreases to 57 emu

$g^{−1}$ at the further increased Zn^{2+} doping amount of $x = 0.6$. The magnetic spin alignment diagrams in Figure 2a illustrate the more intuitive changes in saturation magnetization intensity (M_s value). At a reasonable amount of Zn^{2+} ions ($x < 0.4$) added to the unit cell of a spinel structure, these ions will preferentially occupy the T_d sites, which induces the partial removal of antiferromagnetic coupling interactions between Fe^{3+} ions at the T_d and O_d sites,[19] eventually leading to the increased saturation magnetization. On the contrary, the M_s value of $Zn_{0.6}Mn_{0.4}Fe_2O_4$ of excess Zn doping is much lowered to 57 emu $g^{−1}$ because the antiferromagnetic coupling interaction becomes dominant between Fe^{3+} ions in O_h sites in this case. Furthermore, Figure S2, Supporting Information also shows the significant magnetization enhancement effects of size enlargement.[20] Along with the epitaxial growth of nanoparticles from 8 to 10 and 14 nm (Figure S2a–c, Supporting Information), the M_s value of ZMF nanoparticles also gradually increase from 65 to 71 and 95 emu $g^{−1}$ (Figure S2d, Supporting Information), respectively. The time-dependence of the magnetic separation efficiency determined by Fe-ICP-MS in Figure S3, Supporting Information shows that the magnetic separation rate is almost 100% in 2 min, revealing the excellent magnetic response performance of ZMFS NPs.

Benefiting from the above research, $Zn_{0.4}Mn_{0.6}Fe_2O_4$ NPs of 18 nm in diameter were prepared by a thermal decomposition method[19,21] in the subsequent virus nucleic acid detection for its optimal magnetic performance. The synthesized ZMF shows

**ADVANCED
SCIENCE NEWS**

www.advancedsciencenews.com

**ADVANCED
HEALTHCARE
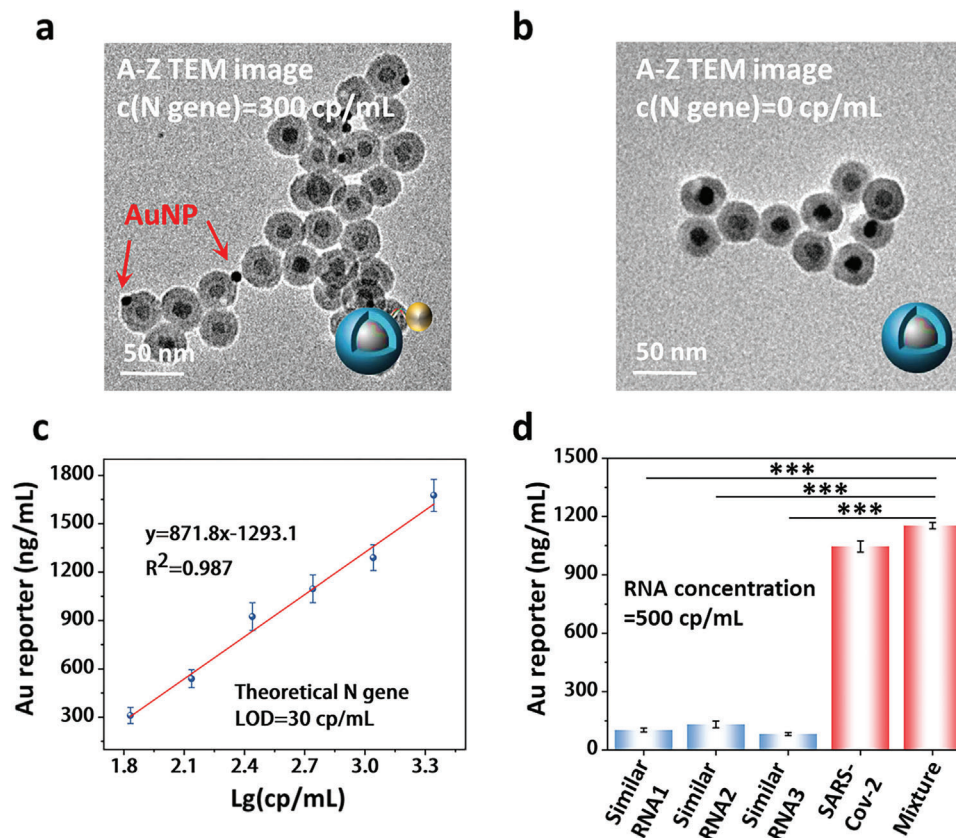MATERIALS**

www.advhealthmat.de

Figure 3. a) TEM image of $Zn_{0.4}Mn_{0.6}Fe_2O_4$ (ZMF) nanoparticles. Inset, DLS size distribution of ZMF nanoparticles in hexamethylene. b) XRD patterns of ZMF (the red line) and Fe_3O_4 nanoparticles (the blue line). c) TEM image of $Zn_{0.4}Mn_{0.6}Fe_2O_4@SiO_2$ (ZMFS) nanoparticles, scale bar: 50 nm. d) EDS elemental mapping images of ZMFS. e) TEM image of Au nanoparticles (AuNPs). f) UV–vis absorption spectra of AuNP (the black line) and AuNP-DNA (the red line). The peak at 267 nm belongs to the absorption by DNA.

excellent monodispersity as shown in the transmission electron microscopy (TEM) image (**Figure 3**a). The well-defined size distribution of ZMF NPs was quantitatively determined in hexamethylene by dynamic light scattering (DLS) (Figure 3a inset), which gives the average hydrodynamic diameter of 16 nm. Both high-resolution transmission electron microscopy (HRTEM, Figure S4, Supporting Information) and X-ray diffraction (XRD, Figure 3b) analysis indicate a well-crystallized FCC spinel structure of ZMF NPs similar to that of Fe_3O_4 NPs. The Zn^{2+} doping amount was practically measured by energy dispersive X-ray spectroscopy (EDS, Figure S5, Supporting Information) and inductively coupled plasma optical emission spectra (ICP-OES, Table S2, Supporting Information). To investigate the chemical state of doped Zn ions in ZMF NPs, X-ray photoelectron spectroscopy (XPS) was applied and the Zn 2p, Mn 2p, and Fe 2p levels of the ZMF sample are shown in Figure S6a–c, Supporting Information. The XPS curve of Zn 2p exhibits a peak at 1022 eV, which can be attributed to the Zn 2p3/2 state corresponding to Zn^{2+} in a spinel structure. Moreover, the XPS curves of both Mn2p and Fe2p present 2p3/2 and 2p1/2 peaks because of spin-orbit interactions, which reveals Mn(II) and Fe(III) components in manganese ferrite structure.[22]

ZMF NPs were then coated with a hydrophilic SiO_2 layer by a Stöber method to improve the long-term stability and biocompatibility of $ZMF@SiO_2$ (ZMFS) NPs for further biomedical ap-

plication (Figure 3c). The Energy-dispersive X-ray spectroscopy (EDS) mapping proves the existences of Zn, Fe, and Mn elements in the ZMF core and homogeneous distribution of Si in the SiO_2 shell layer (Figure 3d), and HRTEM image in Figure S7, Supporting Information further shows a 8 nm-thick SiO_2 shell layer of ZMFS nanoparticles. In order to facilitate the conjugation with carboxyl-modified PNA probes, ZMFS NPs were subsequently amine-functionalized on the surface by aminopropyltriethoxysilane (APTES). Zeta potential analysis in Figure S8, Supporting Information shows that $ZMFS-NH_2$ has a positive zeta potential value of +11.4 mV, while that of ZMFS-PNA is reduced to +6.2 mV due to the introduction of carboxyl-modified PNA probes, suggesting successful conjunction of PNA probes. Herein, PNA probe is a form of synthetic mimics of nucleic acids synthesized by substituting the negatively charged deoxyribose phosphate backbone of DNA with a neutral polyamide backbone (Figure S9a,b, Supporting Information), and PNA can be considered as analogues to metal connectors illustrated in Figure S9c, Supporting Information. Additionally, the monodisperse Au NPs were synthesized by the conventional reduction of $HAuCl_4$ solution with sodium citrate (Figure 3e), and then the DNA sequences complementary to the second half section of target N gene were functionalized on Au NPs by polyA20 block,[23] which are named as Au-DNA (A-D nanoprobe). The UV–vis absorption spectra of Au NPs and Au-DNA in Figure 3f show the typical absorbance at

ADVANCED
SCIENCE NEWS
www.advancedsciencenews.com

ADVANCED
HEALTHCARE
MATERIALS
www.advhealthmat.de

Figure 4. TEM images of A-Z NPs after the hybridization reaction among the designed nanoprobes (A-D and Z-P) and the N gene, magnetic separation and re-dispersion for a) 300 cp mL^{-1} of N gene, and b) 0 ng mL^{-1} of N gene, scale bar: 50 nm. c) Linear correlation between the concentrations of Au reporter (ng mL^{-1}) measured by ICP-MS, and that of SARS-CoV-2 N gene (cp mL^{-1}), for serving as a standard curve. Theoretical limit of detection (LOD) of N gene is 30 cp mL^{-1}. Three parallel samples were set up in each group, and every experiment was repeated for three times. d) NCS complimentary to SARS-CoV-2 was challenged with other three other types of different but similar-sequenced RNA (500 cp mL^{-1}, respectively), and a mixed sample containing both N gene and the three types of RNA at the same 500 cp mL^{-1} for each.

267 nm of DNA, indicating the successful conjugation of DNA onto Au NPs.

As for the SARS-CoV-2 target gene, previous evidence has shown that the SARS-CoV nucleocapsid (N) region is the best target with the highest detection sensitivity.[7a,24] We thus chose the SARS-CoV-2 N gene as an initial detection target to validate the NCS assay reported herein. The complementary sequences of N gene-modified ZMFS-PNA and Au-DNA nanoprobes were designed and evaluated for the sensitivity, detection rate, and specificity of the proposed NCS (**Figure 4**). We first explored the feasibility of the present NCS employing ZMFS-PNA and Au-DNA nanoprobes in detecting N gene sequence in a standard solution. The experimental sample containing N gene (300 cp mL^{-1}) and the control group without N gene target sequence were used to validate the effectiveness of the strategy. After ZMFS-PNA and Au-DNA sensors were hybridized to target N gene sequence, a coupling system of ZMFS-PNA/N gene/Au-DNA containing the target N gene was formed (illustrated in Figure S10, Supporting Information). Upon magnetic separation, the collected product was then redispersed into an aqueous solution and used for TEM observation. According to the TEM imaging (Figure 4a,b), Au is then used as the reporter to evidence the existence of target N gene thanks to the apparent contrast differ-

ence in the TEM Z-contrast images between Au and SiO$_2$ layer on ZMF. As shown in Figure 4a, in the solution containing N gene, the report Au can be clearly seen in the TEM image of the magnetically separated product. In sharp contrast, in a control group containing the same concentration of ZMFS-PNA and Au-DNA nanoprobes but no target N gene, the magnetic separation component shows the complete absence of reported Au NPs (Figure 4b).

Furthermore, duplex hybridization between the nanoprobes and viral RNA was performed to prove the successful hybridization between target N gene and the nanoprobes (ZMFS-PNA/Au-DNA). As illustrated in Figure S11a, Supporting Information, a fluorophore (FAM) was labeled with SARS-CoV-2 N gene at its 5′ and 3′ ends, and ZMFS-PNA and Au-DNA nanoprobes were modified with a quencher Black Hole Quencher (BHQ1). Once ZMFS-PNA-BHQ1 and Au-DNA-BHQ1 hybridize onto N gene-FAM, fluorescence energy of FAM at the 5′ and 3′ end of N gene will transfer to BHQ1, which absorbs and releases the fluorescence energy in the form of heat, leading to quenching of the fluorescence.[25] Figure S11b, Supporting Information shows the fluorescence intensity of N gene-FAM at 520 nm. Following the addition and mixing of nanoprobes in virus sample solution, the fluorescence of N gene-FAM decreased significantly,

**ADVANCED
SCIENCE NEWS**

www.advancedsciencenews.com

**ADVANCED
HEALTHCARE
MATERIALS**

www.advhealthmat.de

indicating the successful hybridization between SARS-CoV-2 RNA and nanoprobes.

We subsequently tested the detection limit of this NCS and linearity between target N gene and Au concentration, which can serve as the standard curve for the quantification of SARS-CoV-2 N gene from the reporter Au concentrations later measured. Several SARS-CoV-2 pseudovirus samples in RNase-free SSPE buffer (pH 7.4) with exponentially varied concentrations (2200, 1100, 550, 275, 137, and 68 cp mL^{-1}) were detected by the present NCS. Corresponding ZMFS-PNA and Au-DNA probes were employed to hybridize to the target N gene sequence to form a three-component coupled ZMFS-PNA/N gene/Au-DNA system. After the magnetic separation, the magnetic-separated product containing the coupled assemblies and the uncoupled ZMFS-PNA NPs were re-dispersed in RNase-free PBS buffer (pH 7.4). The concentrations of Au reporters in the resulting solutions were detected by ICP-MS. The linear relationship between the concentration of the reporter Au and the target N gene (cp mL^{-1}) in the detection system is given in Figure 4c. With the N gene concentration decreasing from 2200 to 68 cp mL^{-1}, the concentration of the reporter Au correspondingly decreased from 1675.3 to 411.8 ng mL^{-1} accordingly (Figure 4c). The linear relationship between N gene concentration and reporter Au readout can be algebraically expressed as $y = 871.8x - 1293.1$ (x: logarithm of N gene concentration to the base 10; y: Au reporter concentration determined by ICP-MS), in which the Au reporter could be used to algebraically amplify the detection signal by more than 870 times. All these results show that the present NCS presents an ultrasensitive detection performance in a very wide N gene concentration range from 68 to 2200 cp mL^{-1} with an excellent linearity ($R^2 = 0.987$). Of note, the theoretical limit of detection (LOD) of N gene is as low as 30 cp mL^{-1}, indicating the ultra-sensitivity NCS assay in the virus detection. Quantitative analyses of SARS-CoV-2 N gene in the presences of other three RNA sequences similar to the N gene further confirm the specificity and sensitivity of this NCS. Briefly, three RNA sequences (NC014470, MG772933, and NC004718) having high percentages of identity (93.75–100%) and query cover (45–85%) with SARS-CoV-2 N gene were synthesized according to the National Center for Biotechnology Information (NCBI). For convenience, all related RNA and probe sequences used in this work are listed in Table S1, Supporting Information. All three RNA samples in the same concentration (500 cp mL^{-1}) were detected by NCS using the corresponding ZMFS-PNA and Au-DNA probes designed for N gene. Following the identical procedures used above for N gene detection, the measured concentrations of magnetic-separated reporter Au for the RNA detections by ICP-MS are shown in Figure 4d. Of note, the final concentration readouts for the solutions containing three similar RNA sequences provide negative results while the solution containing SARS-CoV-2 N gene has an obvious positive outcome. Moreover, the capability of NCS in detecting SARS-CoV-2 N gene in the mixed RNA solution was also determined. A mixed group containing SARS-CoV-2 N gene and the above three kinds of similar sequences at the same concentration (500 cp mL^{-1}, respectively) was detected. As shown in Figure 4d, the mixed gene solution in the same SARS-CoV-2 N gene concentration presents a similar concentration value of reporter Au with that of single SARS-CoV-2 N gene group by this NCS. The above results evidence that a gene-specific oligonucleotide-

Table 1. SARS CoV-2 N gene detection by qRT-PCR and NCS assay.

No.	qRT- PCR		NCS assay	
	C_t value	Calculated N gene [cp mL^{-1}]	Reporter Au [ng mL^{-1}]	Calculated N gene [cp mL^{-1}]
1	39.33	53	372.78	82
2	39.51	47	286.14	65
3	39.95	35	202.8	52
4	38.04	128	579.18	141
5	38.45	98	426.84	94
6	38.78	78	422.82	93
7	36.20	456	1044.42	483
8	35.84	582	1073.7	522
9	36.33	416	991.08	420
10	35.52	723	1245.9	824
11	34.94	1078	1325.04	1016
12	35.28	854	1269	876
13	33.98	2140	1601.94	2116
14	34.11	1900	1561.8	1903
15	34.18	1819	1549.14	1840

functionalized ZMFS-PNA and Au-DNA nanosensors designed for N gene will create no positive signal if used to detect other sequences, because these sequences cannot initiate hybridization reactions with capture DNAs on ZMFS-PNA and Au-DNA NPs which are only complimentary with the SARS-CoV-2 N gene exactly, and also no subsequent nanoparticle-coupling either. These results prove that this NCS are highly sensitive and selective in detecting SARS-CoV-2 N gene in the presence of other types of base sequences even if they are very similar with each other.

To further examine the accuracy and sensitivity of NCS assay, we subsequently compared the present NCS with traditional qRT-PCR which is commonly used in clinical practice. According to the reference SARS-CoV-2 full genomic sequence (NC_045512.2) in GenBank, the synthetic viral sequences of SARS-CoV-2 were obtained from Gene Well Biotech. Co., Ltd. Based on this target SARS-CoV-2 N gene sequence (UUGC UGCU GCUUGA CAGA UU), we designed the complementary capture probes and decorated them on ZMFS and Au NPs for direct recognition of the SARS-CoV-2 N gene sequence (Table S1, Supporting Information). A series of samples at varied concentrations of the pseudovirus of SARS-CoV-2 were prepared and detected by qRT-PCR and our NCS assay, respectively (**Table 1**). In the 15 samples (No.1 to No.15) containing different concentrations of the target SARS-CoV-2 N gene, C_t values of qRT-PCR have been measured to range from 33.98 to 39.95, which are corresponding to the concentrations of SARS-CoV-2 N gene ranging from 35 to 2140 cp mL^{-1} as calculated. In NCS assay, the concentration of reporter Au ranges from 202.8 to 1601.94 ng mL^{-1} determined by ICP-MS, and results of calculated N gene (ranging from 52 to 2116 cp mL^{-1}) are highly consistent with those of qRT-PCR, indicating the excellent accuracy of NCS assay. Of note, in the qRT-PCR testing, the effective linear range of C_t value is within 15–35, but the C_t value presents significant randomness
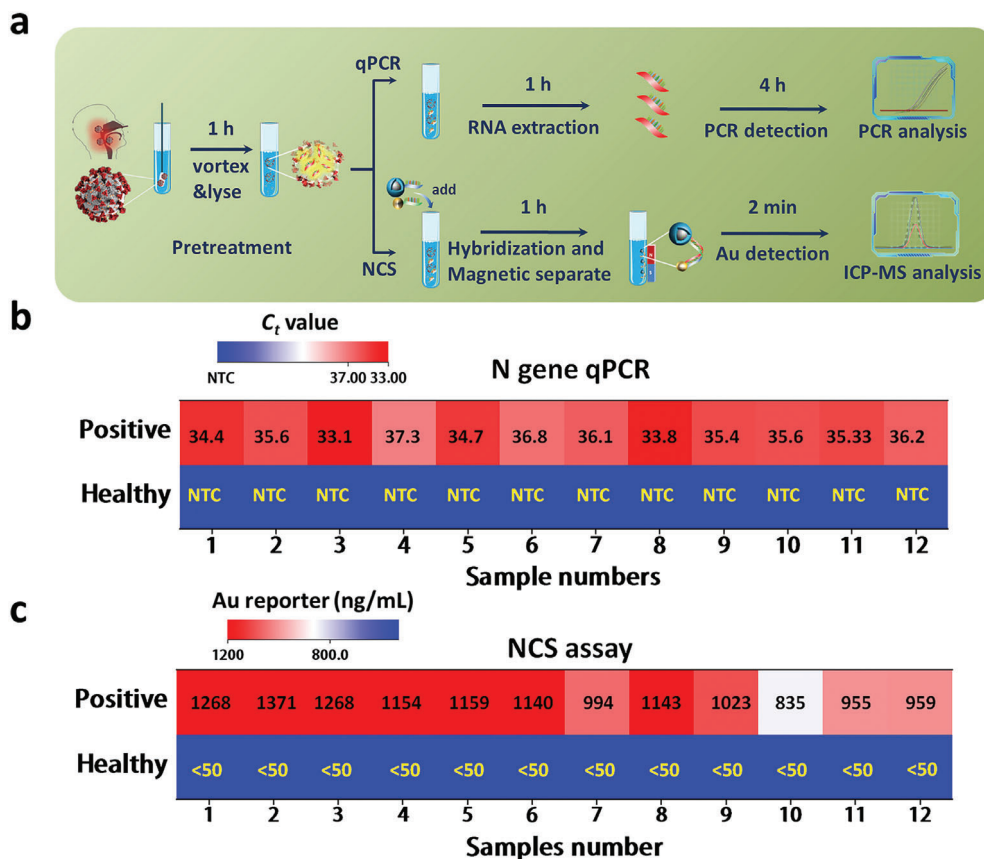
Figure 5. a) The assay procedures of qRT-PCR and NCS. The time intervals above the arrows in (a) indicate the time-consumptions of each step. b) The heat map of C_t values in the blind tests via qRT-PCR. NTC means no template control. c) The heat map of Au reporter concentration in the blind tests via NCS assay.

due to the probability of Poisson distribution at $C_t > 35$, which would cause the significant increase of false positives in clinical testing.[26] In the NCS assay, however, the Au elements are used for the absolute quantification through ICP-MS and the results of samples 1–6 are still within the effective linear range.

The ultimate goal of our effort in establishing and developing the NCS assay is to analyze viral RNA in clinical patient samples. Finally, we evaluated the detection performance of NCS assay using simulative clinical samples. Negative swab samples were obtained from 12 different volunteers. To simulate the positive samples, we spiked different concentrations of the SARS-CoV-2 pseudovirus into the above 12 swab samples, ranging from 500 to 1500 cp mL^{-1} of SARS-CoV-2 N gene. In this way, a cohort ($n = 24$) including 12 negative and 12 positive swab samples was obtained (**Figure 5**). All samples were vortexed and lysed to obtain nucleic acid test solutions. We first examined β-globin as a reference gene to verify the RNA integrity of all samples. The same concentration of RNA samples was used for PCR detection, and resultantly the C_t values of all 24 samples are approximately the same as each other (Figure S12, Supporting Information). For clinical patient samples, several pretreatment steps are necessary before the final detections. The first step is sample vortex and split, which usually takes about an hour. Subsequently, the qRT-PCR assay requires RNA extractions which need another hour. Thanks to the specific recognition ability of capture DNA/PNA

strands-grafted nanoprobes to the target SARS-CoV-2 N gene sequences, NCS assay could hybrid and capture viral nucleic acid in 1 h without additional RNA extractions. Finally, qRT-PCR detection takes at least 4 h to obtain the final test results, including a series of complicated steps such as reverse transcription and enzymatic amplification (Figure 5a). In contrast, with the aid of efficient magnetic separation and enrichment of target RNA and the ultra-low detection limit (1 ng mL^{-1}) of Au ions by ICP-MS, our NCS assay features linear signal outputs from the ultra-low background to maximum amplified level by using Au nanoparticles as reporters and no additional reagent interference. Most intriguingly, no PCR amplification is required and the detection process takes only 2 min (Figure 5a). As illustrated in Figure 5b,c, blind tests of swab samples indicate that NCS assay can clearly discriminate between negative samples ($n = 12$, less than 50 ng mL^{-1}) and positive samples ($n = 12$, ranging from 835 to 1371 ng mL^{-1}). The heat map in the blind test via qRT-PCR is in excellent correspondence with the results of NCS assay, which further proves the reliability of NCS assay for the SARS-CoV-2 N gene detection. Moreover, in detected samples, the results of NCS assay have a remarkably larger data range (ranging from 835 to 1371 ng mL^{-1}) than that in the results of qRT-PCR (C_t values ranging from 33.1 to 37.3), which will largely facilitate the detection rate enhancement of positive samples and false-positive reduction of negative samples.

3. Conclusions

A NCS has been developed based on the hybridization reactions among the prepared nanoprobes ZMFS-PNA and Au-DNA, and target N gene of SARS-CoV-2, for SARS-CoV-2 detection and quantification. Au-DNA conjugation is utilized as signal-transduction agent and ZMFS-PNA acts as separator under magnetic field applied in the NCS. A ZMFS-PNA/target N gene/Au-DNA complex system by the highly specific hybridization reactions enables the following magnetic separation and Au concentration quantification by ICP-MS, finally providing the highly sensitive quantification results. The limit of detection is as low as 52 cp mL^{-1} of SARS-CoV-2 N gene, which is ten times lower than that of clinic PCR method (500 cp mL^{-1}). In addition, the developed NCS assay demonstrates excellent specificity for the virus N gene detection against similar-sequenced counterparts. The present NCS presents extraordinarily high sensitivity and specificity in detecting simulated and patient RNA samples by using nanomaterials as bio-probes, and is therefore readily applicable for detecting clinical patient samples. Further, this NCS strategy is equivalently of great significance for the future monitoring, detection, and prevention of other types of viral epidemics in addition to the current SARS-CoV-2-based COVID-19.

Supporting Information

Supporting Information is available from the Wiley Online Library or from the author.

Conflict of Interest

The authors declare no conflict of interest.

Data Availability Statement

The data that support the findings of this study are available from the corresponding author upon reasonable request.

Keywords

magnetic nanoparticles, nanoprobe-coupling strategy, nucleic acid quick detection, SARS-CoV-2 N gene, Zn^{2+} doping

[1] J. F. W. Chan, S. F. Yuan, K. H. Kok, K. K. W. To, H. Chu, J. Yang, F. F. Xing, J. L. Liu, C. C. Y. Yip, R. W. S. Poon, H. W. Tsoi, S. K. F. Lo, K. H. Chan, V. K. M. Poon, W. M. Chan, J. D. Ip, J. P. Cai, V. C. C. Cheng, H. L. Chen, C. K. M. Hui, K. Y. Yuen, *Lancet* **2020**, *395*, 514.

[2] a) Z. T. Li, Y. X. Yi, X. M. Luo, N. Xiong, Y. Liu, S. Q. Li, R. L. Sun, Y. Q. Wang, B. C. Hu, W. Chen, Y. C. Zhang, J. Wang, B. F. Huang, Y. Lin, J. S. Yang, W. S. Cai, X. F. Wang, J. Cheng, Z. Q. Chen, K. J. Sun, W. M. Pan, Z. F. Zhan, L. Y. Chen, F. Ye, *J. Med. Virol.* **2020**, *92*, 1518; b) M. Sun, S. Liu, X. Wei, S. Wan, M. Huang, T. Song, Y. Lu, X. Weng, Z. Lin, H. Chen, Y. Song, C. Yang, *Angew. Chem., Int. Ed.* **2021**, *60*, 10266.

[3] a) B. Udugama, P. Kadhiresan, H. N. Kozlowski, A. Malekjahani, M. Osborne, V. Y. C. Li, H. M. Chen, S. Mubareka, J. B. Gubbay, W. C. W. Chan, *ACS Nano* **2020**, *14*, 3822; b) X. Jiang, J. C. Loeb, C. Manzanas, J. A. Lednicky, Z. H. Fan, *Angew. Chem., Int. Ed.* **2018**, *57*, 17211.

[4] E. Xiong, L. Jiang, T. Tian, M. Hu, H. Yue, M. Huang, W. Lin, Y. Jiang, D. Zhu, X. Zhou, *Angew. Chem., Int. Ed.* **2021**, *60*, 5307.

[5] Z. Zainol Rashid, S. N. Othman, M. N. Abdul Samat, U. K. Ali, K. K. Wong, *Malays. J. Pathol.* **2020**, *42*, 13.

[6] a) W. L. Wang, Y. L. Xu, R. Q. Gao, R. J. Lu, K. Han, G. Z. Wu, W. J. Tan, *JAMA, J. Am. Med. Assoc.* **2020**, *323*, 1843; b) Y. H. Jin, L. Cai, Z. S. Cheng, H. Cheng, T. Deng, Y. P. Fan, C. Fang, D. Huang, L. Q. Huang, Q. Huang, Y. Han, B. Hu, F. Hu, B. H. Li, Y. R. Li, K. Liang, L. K. Lin, L. S. Luo, J. Ma, L. L. Ma, Z. Y. Peng, Y. B. Pan, Z. Y. Pan, X. Q. Ren, H. M. Sun, Y. Wang, Y. Y. Wang, H. Weng, C. J. Wei, D. F. Wu, et al., *Mil. Med. Res.* **2020**, *7*, 23.

[7] a) V. M. Corman, O. Landt, M. Kaiser, R. Molenkamp, A. Meijer, D. K. W. Chu, T. Bleicker, S. Bruenink, J. Schneider, M. L. Schmidt, D. G. J. C. Mulders, B. L. Haagmans, B. van der Veer, S. van den Brink, L. Wijsman, G. Goderski, J.-L. Romette, J. Ellis, M. Zambon, M. Peiris, H. Goossens, C. Reusken, M. P. G. Koopmans, C. Drosten, *Eurosurveillance* **2020**, *25*, 23; b) J. Deng, F. Tian, C. Liu, Y. Liu, S. Zhao, T. Fu, J. Sun, W. Tan, *J. Am. Chem. Soc.* **2021**, *143*, 7261.

[8] a) N. Li, P. Wang, X. Wang, C. Geng, J. Chen, Y. Gong, *Exp. Ther. Med.* **2020**, *20*, 13; b) A. K. Nalla, A. M. Casto, M.-L. W. Huang, G. A. Perchetti, R. Sampoleo, L. Shrestha, Y. Wei, H. Zhu, K. R. Jerome, A. L. Greninger, *J. Clin. Microbiol.* **2020**, *58*, e00557; c) E. A. Undurraga, G. Chowell, K. Mizumoto, *Infect. Dis. Poverty* **2021**, *10*, 11.

[9] L. Chen, W. Liu, Q. Zhang, K. Xu, G. Ye, W. Wu, Z. Sun, F. Liu, K. Wu, B. Zhong, Y. Mei, W. Zhang, Y. Chen, Y. Li, M. Shi, K. Lan, Y. Liu, *Emerging Microbes Infect.* **2020**, *9*, 313.

[10] J. S. Lian, X. Jin, S. R. Hao, H. Y. Jia, H. Cai, X. L. Zhang, J. H. Hu, L. Zheng, X. Y. Wang, S. Y. Zhang, C. L. Ye, C. L. Jin, G. D. Yu, J. Q. Gu, Y. F. Lu, X. P. Yu, D. R. Xiang, L. J. Li, T. B. Liang, J. F. Sheng, Y. D. Yang, *Influenza Other Respir. Viruses* **2020**, *14*, 564.

[11] A. T. Xiao, Y. X. Tong, S. Zhang, *J. Med. Virol.* **2020**, *92*, 1755.

[12] S. Deka, D. Kalita, *J. Lab. Physicians* **2020**, *12*, 212.

[13] P. Hu, S. J. Zhang, T. Wu, D. L. Ni, W. P. Fan, Y. Zhu, R. Qian, J. L. Shi, *Adv. Mater.* **2018**, *30*, 10.

[14] Z. Yu, P. Hu, Y. Xu, Q. Bao, D. Ni, C. Wei, J. Shi, *Small* **2020**, *16*, 1907233.

[15] J. F. W. Chan, C. C. Y. Yip, K. K. W. To, T. H. C. Tang, S. C. Y. Wong, K. H. Leung, A. Y. F. Fung, A. C. K. Ng, Z. J. Zou, H. W. Tsoi, G. K. Y. Choi, A. R. Tam, V. C. C. Cheng, K. H. Chan, O. T. Y. Tsang, K. Y. Yuen, *J. Clin. Microbiol.* **2020**, *58*, 10.

[16] a) J. Wang, R. Polsky, A. Merkoci, K. L. Turner, *Langmuir* **2003**, *19*, 989; b) B. Amini, M. Kamali, M. Salouti, P. Yaghmaei, *Biosens. Bioelectron.* **2017**, *92*, 679; c) A. Narmani, M. Kamali, B. Amini, H. Kooshki, A. Amini, L. Hasani, *Process Biochem.* **2018**, *65*, 46.

[17] D. Pouliquen, H. Perroud, F. Calza, P. Jallet, J. J. Lejeune, *Magn. Reson. Med.* **1992**, *24*, 75.

[18] T. S. Cheng, J. Pan, Y. Y. Xu, Q. Q. Bao, P. Hu, J. L. Shi, *J. Inorg. Mater.* **2019**, *34*, 899.

[19] J.-t. Jang, H. Nah, J.-H. Lee, S. H. Moon, M. G. Kim, J. Cheon, *Angew. Chem., Int. Ed.* **2009**, *48*, 1234.

[20] W. Wang, Y. Wang, L. Tu, Y. Feng, T. Klein, J.-P. Wang, *Sci. Rep.* **2014**, *4*, 5716.

[21] J. Pan, P. Hu, Y. D. Guo, J. N. Hao, D. L. Ni, Y. Y. Xu, Q. Q. Bao, H. L. Yao, C. Y. Wei, Q. S. Wu, J. L. Shi, *ACS Nano* **2020**, *14*, 1033.

[22] Y. Zhou, X. Tao, G. Chen, R. Lu, D. Wang, M.-X. Chen, E. Jin, J. Yang, H.-W. Liang, Y. Zhao, X. Feng, A. Narita, K. Muellen, *Nat. Commun.* **2020**, *11*, 5892.

[23] W. Lu, L. Wang, J. Li, Y. Zhao, Z. Zhou, J. Shi, X. Zuo, D. Pan, *Sci. Rep.* **2015**, *5*, 10158.

[24] M. Deiana, A. Mori, C. Piubelli, S. Scarso, M. Favarato, E. Pomari, *Sci. Rep.* **2020**, *10*, 18764.

[25] M. K. Johansson, H. Fidder, D. Dick, R. M. Cook, *J. Am. Chem. Soc.* **2002**, *124*, 6950.

[26] M. J. Binnicker, *J. Clin. Microbiol.* **2020**, *58*, e01695.